ADVANCED FUNCTIONAL MATERIALS
www.afm-journal.de

Local Electronic Structure Modulation Enables Fast-Charging Capability for Li-Rich Mn-Based Oxides Cathodes With Reversible Anionic Redox Activity

Xianggang Gao, Haiyan Zhang, Shihao Li, Shuai Zhang, Chaohong Guan, Xiaoping Hu, Juanlang Guo, Yanqing Lai, and Zhian Zhang**

Anionic and cationic redox chemistries boost ultrahigh specific capacities of Li-rich Mn-based oxides cathodes (LRMO). However, irreversible oxygen evolution and sluggish kinetics result in continuous capacity decay and poor rate performance, restricting the commercial fast-charging cathodes application for lithium ion batteries. Herein, the local electronic structure of LRMO is appropriately modulated to alleviate oxygen release, enhance anionic redox reversibility, and facilitate Li^+ diffusion via facile surface defect engineering. Concretely, oxygen vacancies integrated on the surface of LRMO reduce the density of states of O 2p band and trigger much delocalized electrons to distribute around the transition metal, resulting in less oxygen release, enhancing reversible anionic redox and the MnO_6 octahedral distortion. Besides, partially reduced Mn and lattice vacancies synchronously stimulate the electrochemical activity and boost the electronic conductivity, Li^+ diffusion rate, and fast charge transfer. Therefore, the modified LRMO exhibits enhanced cyclic stability and fast-charging capability: a high discharging capacity of 212.6 mAh·g^{-1} with 86.98% capacity retention after 100 cycles at 1 C is obtained and to charge to its 80%, SOC is shortened to 9.4 min at 5 C charging rate. This work will draw attention to boosting the fast-charging capability of LRMO via the local electronic structure modulation.

1. Introduction

Recently, Li-rich Mn-based oxides cathodes (LRMO) written as $xLi_2MnO_3\cdot(1-x)LiTMO_2$ (TM = Nickel, Cobalt and Manganese) have attracted extensive research due to its ultrahigh capacity (>250 mAh·g^{-1}) and low cost in comparison with the commercially employed cathodes.[1] The structure of LRMO is widely recognized as the two phase nanocomposite structure of Li_2MnO_3 phase (space group: *C2/m*) and $LiTMO_2$ phase (space group: *R-3m*). The distinctive honeycomb-like superlattice unit $Li@Mn_6$ in Li_2MnO_3 phase drives from the substitution of 1/3 Li in TM layer, also causing the formation of Li–O–Li connection configuration.[2] As a result, the unhybridized O 2p orbital located at the Li–O–Li configurations can provide extra electrons for charge compensation at high charging voltage (>4.5 V), assigning to the anionic redox chemistry (O^{2-}/O_2^{n-} redox couple, $n < 2$).[3] Unfortunately, irreversible anionic redox such as oxygen loss has caused structural degradation, while contributing to ultrahigh capacity. For example, oxygen release can trigger irreversible migration of transition metal ions, severe side reaction, and harmful crystal structure transformation, resulting in low initial coulombic efficiency, continuous voltage, and capacity decay.[4] Besides, the intrinsic low electronic and ionic conductivity of Li_2MnO_3 phase and sluggish kinetic of oxygen redox restrain the rate performance and deteriorate the fast-charging capability of LRMO.[5] Therefore, it is urgent to find an effective strategy to alleviate irreversible oxygen loss, activate reversible oxygen redox, and simultaneously facilitate the fast electrochemical kinetics of LRMO, especially considering its upcoming application in the electric vehicle field.

In order to address the above issues, plenty of modification strategies including surface coating, elemental doping, and surface defect/heterostructure engineering have been raised to suppress oxygen loss, severe side reaction, and layered to spinel phase transformation for achieving excellent electrochemical performance in recent years.[5a,6] Compared with surface coating and elemental doping, surface defect engineering can be easily achieved without the introduction of foreign impurities or

X. Gao, H. Zhang, S. Li, S. Zhang, J. Guo, Y. Lai, Z. Zhang
School of Metallurgy and Environment
Hunan Province Key Laboratory of Nonferrous Value-Added Metallurgy
Engineering Research Center of the Ministry of Education for Advanced Battery Materials
Central South University
Changsha, Hunan 410083, P. R. China
E-mail: laiyanqingcsu@163.com; zhangzhian@csu.edu.cn

H. Zhang
Hunan Changyuan LiCo Co., Ltd
Changsha, Hunan 410205, P. R. China

C. Guan
University of Michigan-Shanghai Jiao Tong University Joint Institute
Shanghai Jiao Tong University
800 Dongchuan Road, Shanghai 200240, P. R. China

X. Hu
School of Materials Science and Engineering
Central South University
Changsha, Hunan 410083, P. R. China

The ORCID identification number(s) for the author(s) of this article can be found under https://doi.org/10.1002/adfm.202304065

DOI: 10.1002/adfm.202304065

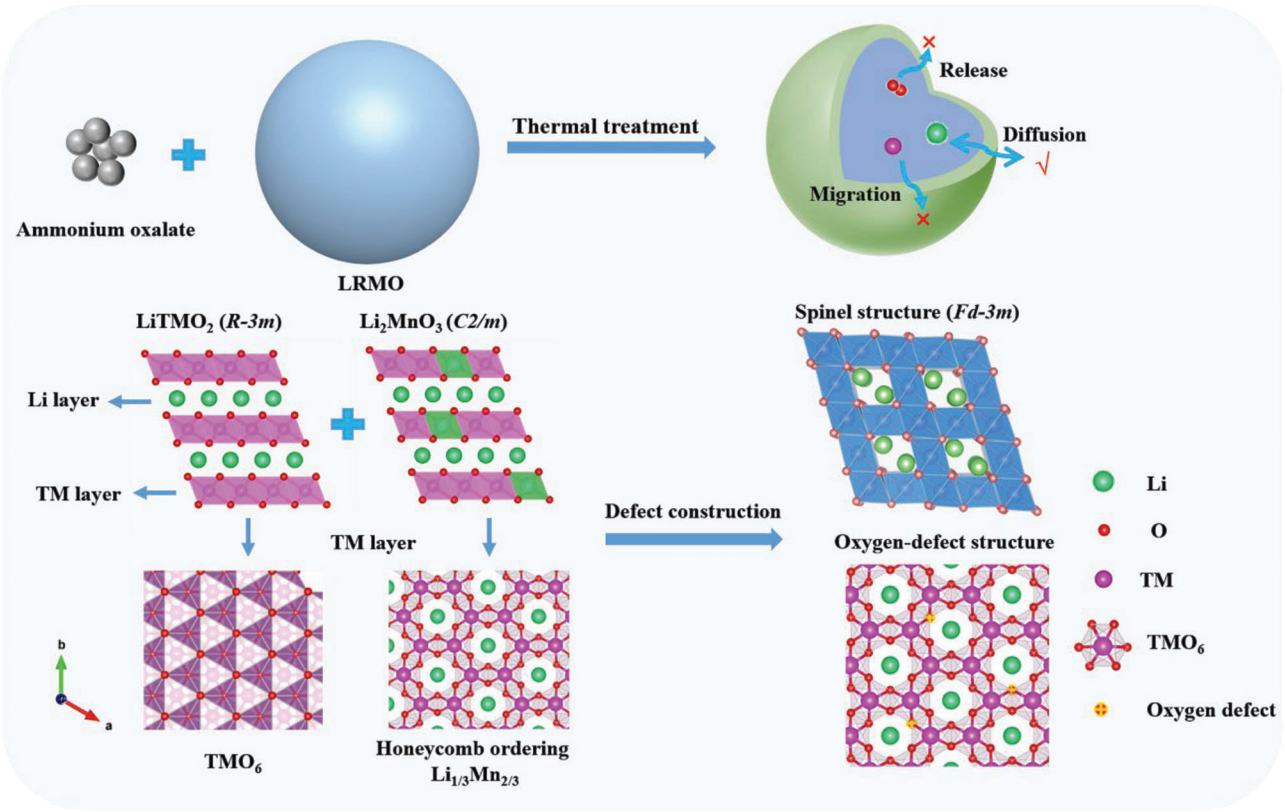

Figure 1. Schematic of surface defect engineering and the transformation of surface crystal structures for LRMO materials.

inactive substances. Therefore, surface defect engineering has received wide attention in the past few years. Surface defects such as lithium and oxygen vacancies can be incorporated into the crystal structure during the synthesis process or subsequent modifications. Surface defects usually enable to modulate the local electronic structure or atomic coordination environment, contributing to activate reversible anionic redox, suppress irreversible oxygen release and structural deterioration. For example, lithium defect can be incorporated on the surface structure of LRMO and trigger the generation of spinel-like phase coating via changing the usage of Li salt, beneficial for enhancing the rate performance and cycling stability.[7] Recently, Zhang et al. further disclosed that lithium defects were able to regulate the 3d-transition metal interlayered disorder, contributing to the stable crystal structure with low energy and Li^+ diffusion barrier.[8] Therefore, Co-free lithium-rich cathode with a long-neglected Li-deficient state exhibited enhanced capacity, improved initial efficiency, and excellent cyclic stability. Furthermore, oxygen vacancy, as one of the conventional defect structures, has been widely studied in the layered oxides cathodes of lithium or sodium ion batteries. Previous works have demonstrated that oxygen defect can suppress oxygen release and irreversible phase transformation and accelerate the electrical conductivity and lithium ion diffusion rate.[9] For example, Li et al. incorporated oxygen vacancy on the surface of LRMO for inhibiting the irreversible evolution of lattice oxygen via hydrogenation treatment.[6c] The results demonstrated that oxygen vacancy can enhance the cyclic stability of LRMO. In addition, Zhang et al. constructed oxygen vacancy and $Li_4Mn_5O_{12}$ on the surface of Li-rich oxide layered cathodes by using a facile oxalic acid assisted delithiation process.[10] The irreversible release of oxygen and voltage decay were obviously alleviated. Therefore, surface defect engineering is a direct and feasible way for tuning the lattice oxygen redox and suppressing the irreversible oxygen loss. Nevertheless, to the best of our knowledge, few study and detailed analyses pay attention to boost the kinetics of reversible anionic redox and fast-charging capability for LRMO materials via surface defect engineering.

Herein, as shown in **Figure 1**, a moderate surface defects construction strategy with ammonium oxalate thermal treatment is successfully realized for manufacturing oxygen vacancies and spinel-like structure on the surface. The underlying mechanisms of surface defect structure on enhancing the cyclic stability, reversible oxygen redox, and fast-charging capability are revealed by different characterizations. Oxygen vacancies are able to modulate the local electronic structure via decreasing the density of states of O 2p band and increasing the delocalized electrons to distribute around the transition metal, which is beneficial for precluding the release of oxygen, enhancing reversible oxygen redox and improving the MnO_6 octahedral distortion. Moreover, under the synergistic function of oxygen vacancies and partial reduced Mn, the electrochemical activity of Li_2MnO_3 phase is effectively stimulated with increasing electrical conductivity and fast charge transfer. In addition, the spinel phase possessing 3D Li^+ channels embedded in the surface of LRMO can also accelerate the Li^+ diffusion rate. As a result, the modified material displays improved

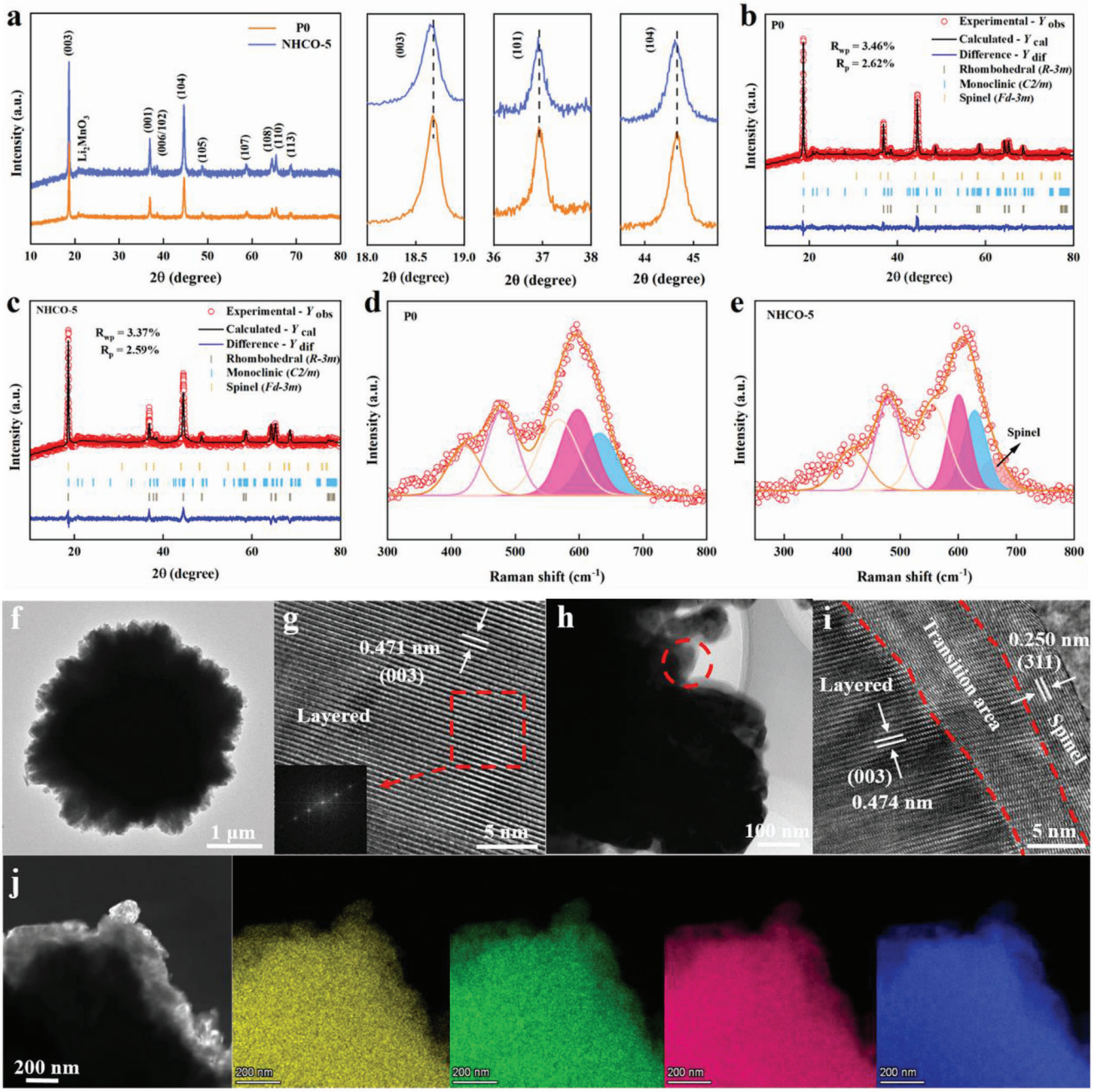

Figure 2. a) The XRD patterns of P0 and NHCO-5 samples with the enlarged images of (003), (101), and (104) peaks, respectively. Refined XRD data of b) P0 and c) NHCO-5. Raman spectra of d) P0 and e) NHCO-5. The TEM and HRTEM images of f,g) P0 and h,i) NHCO-5. j) STEM-EDS mapping of Ni, Co, Mn, and O elements of NHCO-5 samples.

cycling performance with excellent rate performance and fast-charging capability. The present work provides some references to enhance fast-charging capability of LRMO with reversible anionic redox via surface defect engineering.

2. Results and Discussion

Li-rich Mn-based oxides cathodes treated with 3wt%, 5wt%, and 8wt% of ammonium oxalate are denoted as NHCO-3, NHCO-5, and NHCO-8 samples, respectively. The pristine LRMO without any modification is marked as P0 sample. **Figure 2**a shows the XRD patterns of P0 and NHCO-5 samples. The narrow and sharp peaks of both the samples demonstrate the good crystallinity. The apparent peaks belonging to the hexagonal α-$NaFeO_2$ structure with space group *R-3m* can be observed. Several weak peaks located at ≈20–25° are assigned to the monoclinic Li_2MnO_3 phase with space group *C2/m*, possessing the unique superlattice honeycomb ordering structure[22]. No new phase is found after

ammonium oxalate thermal treatment. What is more, the well splitting of (006)/(102) and (108)/(110) peaks for all the samples demonstrates the well-formed layered ordering structure without any destruction after surface modification treatment. The value of I(003)/I(104) of all the samples is larger than 1.2, indicating the low cation mixing.[11] In addition, the left-shift peaks of (003) and (104) ascribe to the enlarged d-spacing and Li^+ slab, ascribing to the extraction of oxygen atoms after surface defect construction.[9b,12] The increasing interplanar spacing is beneficial for the fast Li^+ diffusion and to enhance the fast-charging capability. Meanwhile, the shoulder (101) peak indicates the existence of spinel phase.[13] Figure 2b,c; Figure S1c,d, Supporting Information, shows the results of Rietveld refined XRD data of all the samples, and the detailed refined lattice parameters are listed in Table S1, Supporting Information. The increasing *c* value conforms to the left-shift of (003) peak in XRD pattern. Moreover, the decrease of Li_2MnO_3 phase and the increase of spinel phase further demonstrate that the spinel phase originates from the reaction of Li_2MnO_3 phase with the products of ammonium oxalate pyrolysis. Raman spectra is also performed to detect the local structure as it is sensitive to the short-range ordering and beneficial for phase identification. The fitting results of Raman spectra are displayed in Figure 2d,e; Figure S1e,f, Supporting Information. The peaks around 479 and 597 cm^{-1} belong to the E_g and A_{lg} vibrations of $LiTMO_2$ component.[5a] The peaks of 420 and 632 cm^{-1} are ascribed to Li_2MnO_3 constituent. The additional peak around 660 cm^{-1} after ammonium oxalate treatment appears due to the formation of the spinel-like structure.[5a,14] These results further demonstrate the appearance of spinel phase due to the in situ atomic structure rearrangement after surface treatment. Incorporating spinel-like structure with 3D Li ions diffusion tunnel on the surface of modified materials can promote the fast Li^+ diffusion and alleviate the irreversible structural transformation.[15] The modified materials possess similar coral-like morphology with the pristine materials except for the denser surface as shown in Figure S2a–h, Supporting Information, which can reduce the contact area between materials and electrolyte to alleviate side reaction and enhance cycling stability.

Further, transmission electron microscopy (TEM) and high-resolution TEM (HRTEM) characterizations were conducted to explore the surface crystal structure changes after surface modification. The relevant results are depicted in Figure 2f–j. Both the P0 and NHCO-5 samples show clear lattice stripe, indicating a perfect crystal structure. Figure 2g depicts the HRTEM images of P0 samples driving from the Figure 2f. A classic interplanar spacing of 0.471 nm corresponding to (003) facet of layer structure with *R*-$\bar{3}$*m* space group can be found, which is also demonstrated by the fast Fourier transform (FFT) analysis (a local FFT of the rectangular area in Figure 2g).[16] In contrast, an enlarged interplanar spacing of 0.474 nm in bulk can be detected in Figure 2i (enlarged TEM images of circular area in Figure 2h), conforming to the above XRD results. In addition, a narrow interplanar spacing of 0.250 nm in the outside of surface belongs to the (311) lattice planes of the spinel phase with *Fd–3m* space group being clearly observed.[17] Transition area located between the bulk and surface area is referred to the layered-spinel growth structure, indicating that the migration of transition ions to the Li layer triggers the surface structure rearrangement and formation of spinel phase.[17b] The enlarged d-space and integrated spinel structure can boost the fast Li^+ diffusion, enhance the rate performance and fast-charging capability of LRMO. These results provide strong evidences of the existence of spinel phase, well consistent with the results from XRD and Raman analysis (Figure 2a,e). EDS mapping under high resolution shows the uniform elemental distribution of NHCO-5 samples (Figure 2j), indicating that surface defect engineering does not change the uniform distribution of Ni, Co, Mn, and O elements.

Surface defect engineering usually can result in the obvious changes of elemental chemical compositions and metal valence, exerting a significant impact on the electrochemical properties of LRMO. Therefore, relevant characterizations such as XPS, EPR, and XAS were carried out for detecting these specific changes, and the corresponding results were depicted in **Figure 3**; Figure S4, Supporting Information. The peaks of 531.54 and 529.55 eV in the XPS spectra of O 1s contributed to the oxygen vacancies and lattice oxygen, respectively.[6c,10] The content of oxygen vacancies increased with the increasing usage of ammonium oxalate as displayed in Figure 3a,b; Figure S4a,b, Supporting Information. Moreover, the EPR signal intensity of NHCO-5 was also much higher than P0 in Figure 3c, further proving the increasing of oxygen vacancies on the surface.[18] Further, the O K-edge XANES spectra of NHCO-5 in TEY mode showed an obvious decrease of pre-edge peak overall intensity in comparison with P0 (Figure 3d), ascribing to the formation of surface oxygen vacancies.[19] Therefore, these results have directly demonstrated that oxygen defects are successfully constructed on the surface of NHCO-5 sample via ammonium oxalate treatment. The surface oxygen defects are able to suppress oxygen release and structural deterioration. The possible formation mechanism of oxygen defects is that the decomposed NH_3, CO, and CO_2, deriving from the pyrolysis of ammonium oxalate, can induce the formation of oxygen vacancies via extracting lattice oxygen under high temperature.[9b,20] Figure 3e,f shows the Mn 2p peak of P0 and NHCO-5, respectively. The larger area of Mn^{3+} peak in comparison with P0 indicates that partial Mn is reduced from the Mn^{4+} to Mn^{3+}. In addition, the multiple splitting of Mn 3s XPS spectra analysis can further be used to calculate the changes of the average valence state of Mn. Figure 3g shows that the Mn 3s peak splitting has been increased from 4.43 to 5.02 eV after ammonium oxalate treatment, equaling to the reduction of Mn valence state from 3.88 to +3.29, calculated from the empirical Equation (S1), Supporting Information. The result also further demonstrates the generation of spinel structure due to the increasing low valence of Mn, corresponding to the results of XRD, Raman, and HRTEM analysis. What is more, partially reduced Mn on the surface can activate the Li_2MnO_3 phase and promote the cation to participate in charge compensation.[21] Besides, the valence of Ni and Co shows little change in comparison with Mn, as displayed in Figure S4, Supporting Information, contributing to the fact that ammonium oxalate mainly reacts with Li_2MnO_3 components.

With respect to electrochemical performance, to evaluate the cyclic stability, rate performance, and fast-charging properties of P0 and NHCO-5, all the assembled electrodes are initially activated at a low rate of 0.1 C rate test for three cycles (1 C = 250 mAh g^{-1}, ≈2.0–4.8 V, 25 °C). Typical initial charge–discharge curves of LRMO can be observed for both P0 and NHCO-5 electrodes (Figure S5a, Supporting Information): a sloped region

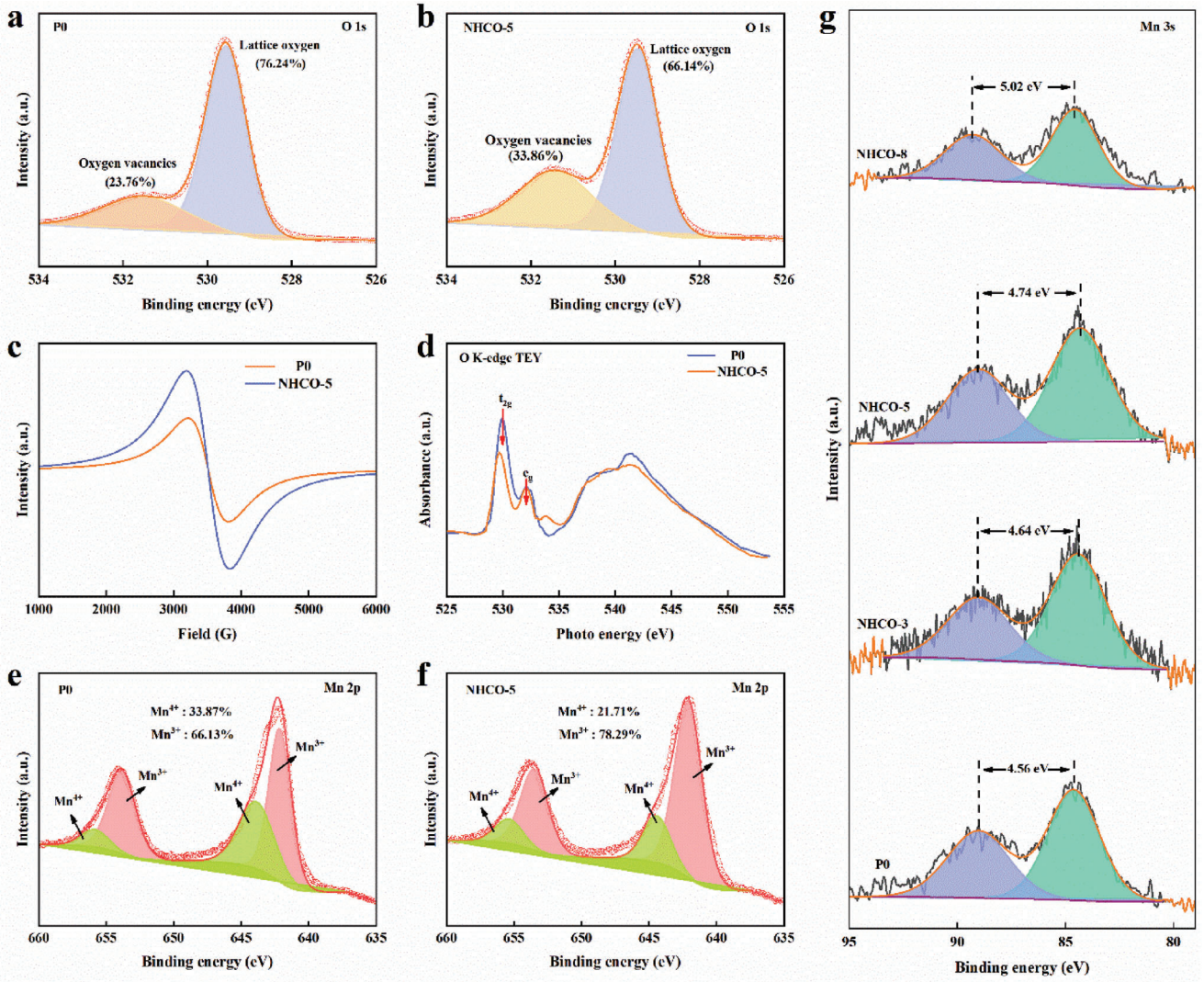

Figure 3. High-resolution XPS spectra of O 1s for a) P0 and b) NHCO-5. c) EPR spectra of P0 and NHCO-5. d) Normalized O K-edge sXAS spectra of P0 and NHCO-5. The XPS spectra of Mn 2p for e) P0 and f) NHCO-5. g) The XPS spectra of Mn 3s for P0, NHCO-3, NHCO-5, and NHCO-8.

(<4.5 V) and a long plateau (≈4.5 V) correspond to the oxidation process of transition metals and electrochemical activation of Li_2MnO_3, respectively.[22] In contrast, NHCO-5 electrode delivers increasing discharging capacity with a higher ICE (297.0 mAh·g^{-1}, 82.29%) than P0 (279.5 mAh·g^{-1}, 77.13%), indicating better reversible anionic redox. As the voltage is charged above 4.5 V, lattice oxygen will be oxidized to $O_2{}^{n-}/O_2$ and removed from the Li_2MnO_3 phase for charge compensation. Thereby, an obvious oxidization peak appears around 4.5 V at the initial dQ/dV curves. Such peak intensity of P0 in Figure S5b, Supporting Information, is the highest in comparison with other samples, suggesting a serious problem of oxygen release.[23] The peak of oxygen oxidization is weakened with the increased usage of ammonium oxalate, demonstrating the release of oxygen is inhibited to some extent. The constant current and constant voltage charge–discharge curves of P0 and NHCO-5 samples at different rates are depicted in **Figure 4**a,b. The capacities of P0 electrode are 272.8, 250.1, 225.1, 200.6, 166.5, and 117.5 mAh·g^{-1} at rates of 0.1, 0.2, 0.5, 1, 2, and 5 C, respectively. However, NHCO-5 electrode exhibits superior rate performance with low voltage polarization. The capacities of NHCO-5 electrode are 292.9, 278.1, 256.7, 240.7, 219.9, and 180.7 mAh·g^{-1} at rates of 0.1, 0.2, 0.5, 1, 2, and 5 C, respectively, which are much higher than the values of P0 electrode (Figure 4c). The enhanced rate performance is suitable for the commercial application of fast-charging lithium ion batteries. As anticipated, the NHCO-5 electrode exhibits excellent cyclic stability due to the enhanced anionic redox and alleviation of oxygen release after surface treatment: high initial reversible discharging capacity of 244.4 and 212.6 mAh·g^{-1} with capacity retention of 86.98% after 100 cycles at 1 C can still be obtained (Figure 4d).

To further examine the fast-charging properties of modified material, both the electrodes were charged at 3 or 5 C and discharged at 1 C for the fast-charging performance assessment. Figure 4e–i; Figure S5c–f, Supporting Information exhibits the relevant electrochemical results. Figure 4e,f; Figure S5c,d,

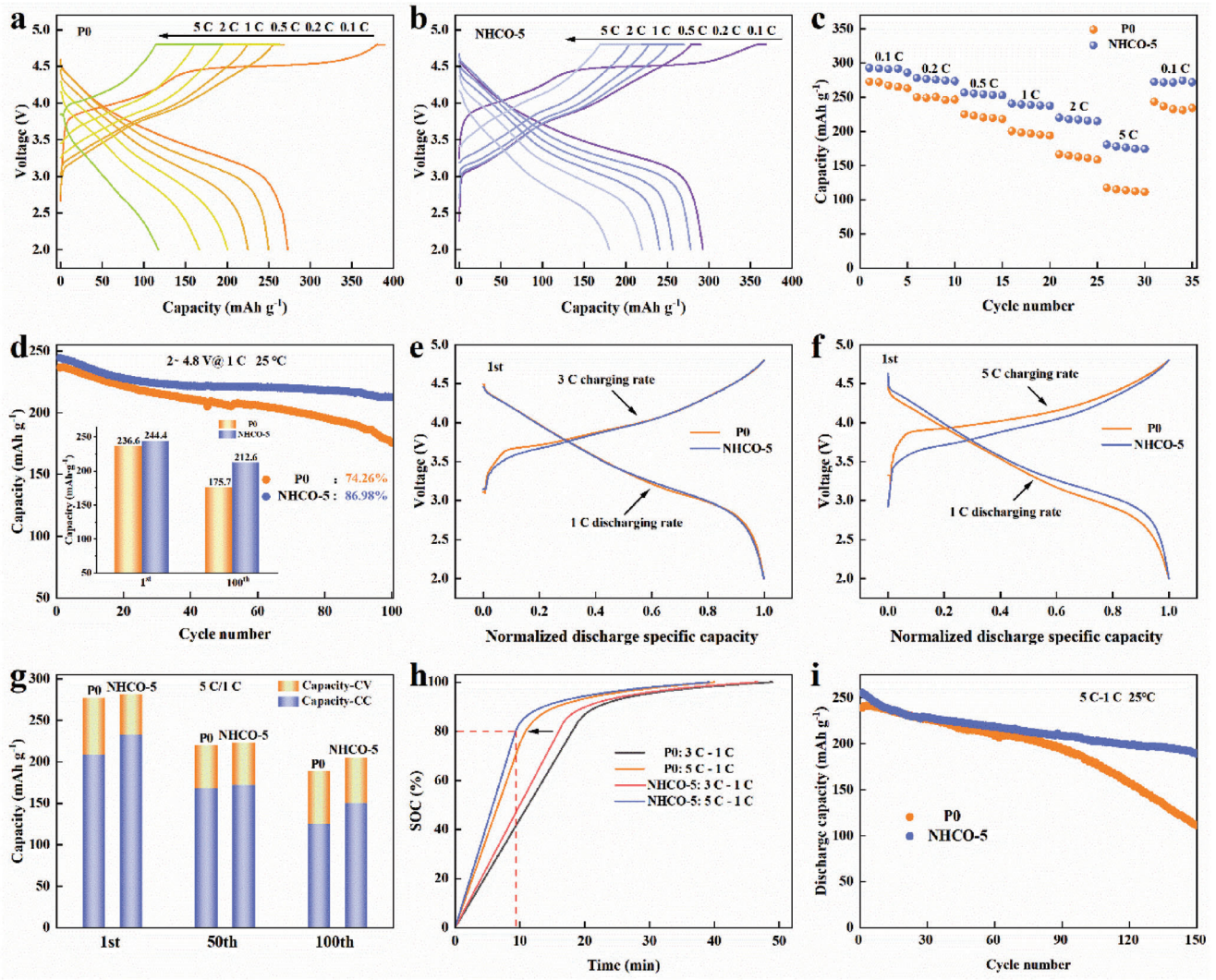

Figure 4. The electrochemical performance of P0 and NHCO-5 electrodes: charge–discharge curves of a) P0 electrode and b) NHCO-5 electrode. c) The rate performance. d) Cycling performance. The initial charge and discharge curves at e) 3 C and f) 5 C fast charging rate after three cycle activation. g) Constant current and voltage of charging capacity obtained from the 1st, 50th, and 100th at 5 C charging rate. h) Charging SOC versus time curves at 3 C and 5 C. i) Cycling performance at 5 C charging rate and 1 C discharge rate.

Supporting Information, shows the first and last charge and discharge curves at 3 and 5 C charging rate, respectively. There is no obvious difference as charged at 3 C for the two electrodes. However, P0 electrode shows larger voltage polarization as charged at 5 C in comparison with NHCO-5 electrode, indicating surface defect and spinel phase can reduce voltage polarization. The capacity of P0 and NHCO-5 electrodes obtained from constant current charging (CC-Capacity) and constant voltage charging (CV-Capacity) section at 3 and 5 C rate are shown in Figure S5e, Supporting Information; Figure 4 g, respectively. To charge more capacity during the constant current charging state can shorten the total charging time. The charging capacity of P0 and NHCO-5 electrodes driving from CC-Capacity and CV-Capacity show less difference as charged at 3 C. However, higher capacity of NHCO-5 electrode can be obtained from the CC-Capacity section than P0 electrode at 5 C fast-charging rate. Consequently, the time to charge 80% SOC capacity of NHCO-5 can be shortened to 9.4 min and less than P0 (≈11 min), as seen in the Figure 4h. Figure S5f, Supporting Information; **Figure 5**i show the comparison of the cycling performance of P0 and NHCO-5 electrodes at 3 and 5 C fast-charging rate. P0 and NHCO-5 electrodes have similar initial charging capacity and show little difference on capacity loss as cycled at 3 C fast-charging rate after 100 cycles. Nevertheless, NHCO-5 electrode still can deliver high reversible initial discharged capacity of ≈250 mAh·g^{-1} and obtain a reversible capacity of 189.4 mAh·g^{-1} as cycled at 5 C after 150 cycles. These results have clearly demonstrated that the 5 C fast charging capability of LRMO is enhanced after ammonium oxalate treatment. The surface spinel phase provides a 3D lithium-ion channel with fast Li^+ diffusion, and oxygen vacancies can synergistically improve the electronic and ionic conductivity of LRMO.[9b,17c] Therefore, the increasing fast-charging capability is ascribed to the enhanced diffusion kinetic and fast charge transfer after the local electronic structure modulation via surface defect engineering.[24]

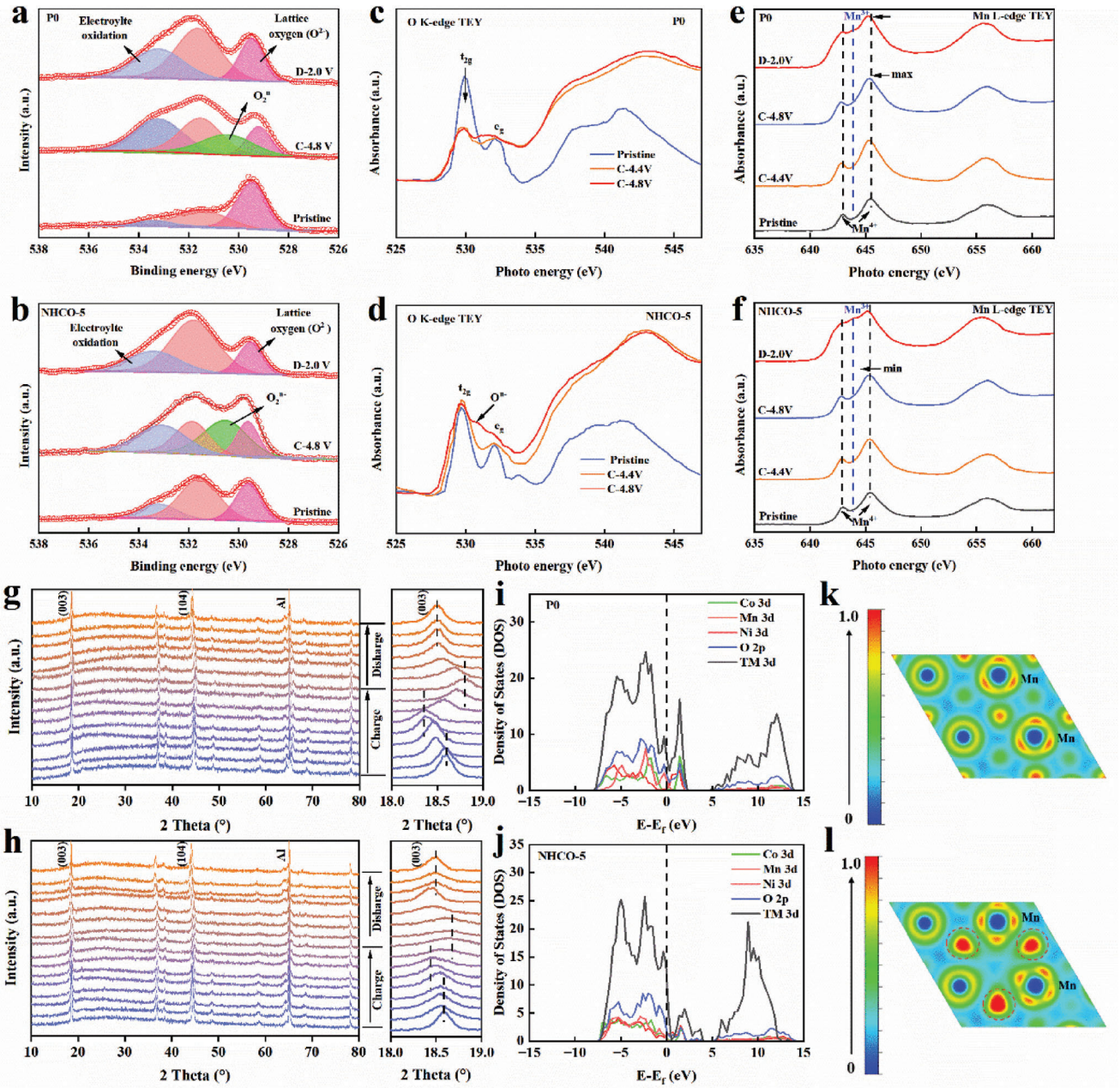

Figure 5. The O 1s XPS spectra at different charging/discharging states of a) P0 electrode and b) NHCO-5 electrode. The normalized O pre K-edge and Mn pre L-edge XAS spectra for c,e) P0 electrode and d,f) NHCO-5 electrode. Ex situ XRD patterns of g) P0 electrode and h) NHCO-5 electrode in the initial cyclic process. Density of states of the i) P0 and j) NHCO-5 sample. Maps of ELF for the k) P0 and l) NHCO-5; circles show there are more delocalized electrons around the transition metal.

As far as mechanisms of the improved rate performance and fast-charging capability are concerned, previous reports have demonstrated that oxygen redox chemistry results in sluggish kinetics with low Li^+ diffusion rate and high charge-transfer resistance.[5c,25] Therefore, tuning anionic redox chemistry plays a vital role in raising the electrochemical performance with excellent fast-charging capability. EIS and the GITT were employed to measure the kinetic variation before and after the electronic structure modulation. Figure S6a, Supporting Information shows the EIS Nyquist plots of P0 and NHCO-5 electrodes before electrochemical cycles. All the curves include three regions. A small interrupt in the high frequency represents the Ohmic resistance (R_s) of the cell. One semicircle in the middle-high frequency represents the charge transfer resistance (R_{ct}). A sloping line in the low-frequency regions represents the Warburg impedance (W).[10] The related fitting parameters are listed in Table S2, Supporting Information. The R_{ct} of NHCO-5 is 7.525 Ω smaller than P0 (9.660 Ω), demonstrating a low charge transfer

impedance of NHCO-5 with surface defect construction.[17c] The GITT measurement is also conducted to compare the kinetic performance of P0 and NHCO-5 electrodes after five cycles at 0.04 C (Figure S6b, Supporting Information). Figure S6c,d, Supporting Information, show the calculated D_{Li}^+ of the charging and discharging process according to the Equation (S2), Supporting Information. The D_{Li}^+ of the NHCO-5 electrode in "sluggish kinetic region" (<3.5 V and >4.0 V) is increased in comparison with P0. The average D_{Li}^+ of NHCO-5 electrode in "sluggish kinetic region" is 8.70×10^{-10} cm^2 s^{-1} and 6.40×10^{-10} cm^2 s^{-1} during charging process and discharging process respectively, which is larger than the values of 5.97×10^{-10} cm^2 s^{-1} and 4.56×10^{-10} cm^2 s^{-1} for P0 electrode. The improved lithium diffusion rate and fast charge transfer, ascribing to the local electronic structure modulation, result in boosting the rate performance and fast-charging capability of LRMO.

The O 1s XPS spectra of P0 and NHCO-5 electrodes at charging and discharging state in the first cycle are conducted for exploring the mechanisms of oxygen redox (Figure 5a,b). Three obvious peaks appearing at ≈529.5, ≈531.9, and ≈533.2 eV contributing to the lattice oxygen, oxygenated deposited species, and weak electrolyte oxidation, respectively, whether in the charging state of 4.8 V or discharging state 2.0 V, can be found.[26] However, an additional peak at ≈530.5 eV appears in both the XPS spectra of P0 and NHCO-5 electrodes at the charging state of 4.8 V, contributing to the preoxo-like O_2^{n-} ($n < 2$) with a lower electronic density in comparison with lattice oxygen (O^{2-}).[9a] Nevertheless, compared with P0 electrode, the larger area ratio of O_2^{n-} peak in NHCO-5 electrode indicates more reversible anionic redox participation in charge compensation. It is worth noting that the increasing content of electrolyte oxides at 4.8 V for both P0 and NHCO-5 electrodes can be ascribed to the side reaction and decomposition of electrolyte at high voltage.[27] The disappearance of the preoxo-like O_2^{n-} peak after discharging to 2.0 V indicates the O_2^{n-} can convert back to O^{2-}.[28] These results perfectly demonstrate that the existence of oxygen vacancies in the NHCO-5 electrode can greatly stimulate the reversible anionic redox activity. In addition, soft X-ray absorption spectroscopy (sXAS) can prove the reversible oxygen redox and irreversible oxygen release. The total d electronic holes in the hybridized O 2p-TM 3d can be reflected in the pre-edge peaks of O K-edge spectra at ≈530 eV. The pre-edge peak of P0 electrode largely reduces during charging process, which may be ascribed to the Mn reduction resulting from oxygen loss (Figure 5c). Previous works have proved that the oxidation of lattice oxygen can trigger the charge transfer from oxygen to TM with release of oxygen.[29] The decreasing density of electronic holes in O 2p-Mn 3d due to the reduction of Mn can weaken the O k-edge pre-edge peaks. However, the intensity of pre-edge peaks for charged NHCO-5 electrode shows no obvious changes in comparison with the initial state, indicating the inhibition of oxygen release (Figure 5d). Besides, a new peak located at around 530.5 eV in NHCO-5 electrode is speculated to be the characteristic peak of reversible anionic redox (O^{2-} to O_2^{n-}), conforming to the results of XPS.[5b] Figure 5e,f shows the Mn L-edge XAS spectra at different states for P0 and NHCO-5 electrodes. Compared with NHCO-5 electrode, the peak at around 646.5 eV contributes to Mn^{4+} for P0 electrode shifts more to low energy, indicating the reduction of Mn due to the irreversible oxygen release.[19] Therefore, both the XPS and XAS results successfully demonstrate the surface oxygen vacancies, and spinel phase can enhance the reversible anionic redox and suppress irreversible oxygen release.

Ex situ XRD is applied to figure out the influence of the surface treatment on the crystal structural evolution of LRMO. The associated results are displayed in Figure 5g,h. The shift of (003) peak can directly reflect the changes of lattice parameter *c* value. Both P0 and NHCO-5 electrodes show similar shift direction during the charging and discharging process. Before the voltage is charged to 4.5 V, the peak of (003) shifts to a low angle, indicating the increasing crystal plane spacing due to the increasing electrostatic repulsion and the expansion of the *c*-axis after the removal of Li^+ from the $LiTMO_2$ phase.[3a] After the voltage reaches to 4.8 V, the peak of (003) shifts to a high angle, which derives from the activation of Li_2MnO_3 phase. The lattice oxygen release of Li_2MnO_3 phase causes the decrease of electrostatic repulsion, inducing the TM to migrate into the Li layer.[30] During the discharging process, the peak shifts to left due to the expansion of the crystal plane spacing after the intercalation of Li^+. According to the above analysis, the shift angle of the (003) peak for NHCO-5 electrode is always smaller than that of P0 electrode during both the charging and discharging process, indicating better structural stability and less oxygen release. In addition, the (003) peak of NHCO-5 electrode at full discharging state is closer to the initial position in comparison with P0 electrode, demonstrating that less irreversible phase transformation occurs in the NHCO-5 electrode. Therefore, these results successfully prove that oxygen vacancies can enhance the structural stability and suppress lattice oxygen loss, which is the foundation for achieving fast-charging properties with reversible oxygen redox.

To further demonstrate and understand the influencing mechanisms of surface defect structure on the electrochemical performance, first principles calculations are conducted for studying the electronic structure of P0 and NHCO-5 according to the density functional theory method (DFT). Figure S7a,b, Supporting Information, shows the computational model, and one oxygen vacancy is chosen in the model of NHCO-5. According to this model, the density of states of O 2p and TM 3d band for P0 and NHCO-5 are first computed. Figure 5i,j shows the corresponding computational results. The obvious electron density of TM 3d and O 2p close to the Femi energy indicate that both the P0 and NHCO-5 possess good electrical conductivity.[10] Nevertheless, a careful comparison shows that the density of O 2p band of NHCO-5 decreases in comparison with P0. The decrease of O 2p density can promote lattice oxygen to participate in the charge compensation stably and preclude the oxygen loss, contributing to the enhanced reversible anionic redox.[31] Figure 5k,l displays the isosurface images of electron localization function (ELF), which can clearly depict the cationic charge compensation. The red and light blue regions represent the lattice electrons and active covalent electrons, respectively. The P0 show more localized electrons around the oxygen and transition metal (Figure 5k). In contrast, more delocalized electrons appear around Mn in the NHCO-5, as shown by the red dashed coil in Figure 5l. The change of the local electronic structure around the Mn ion can improve the Mn octahedral distortion reversibility and promote the reduced Mn to participate in the charge compensation.[28,32] Therefore, the surface oxygen defect can modulate the electronic structure around oxygen and Mn, resulting in not only

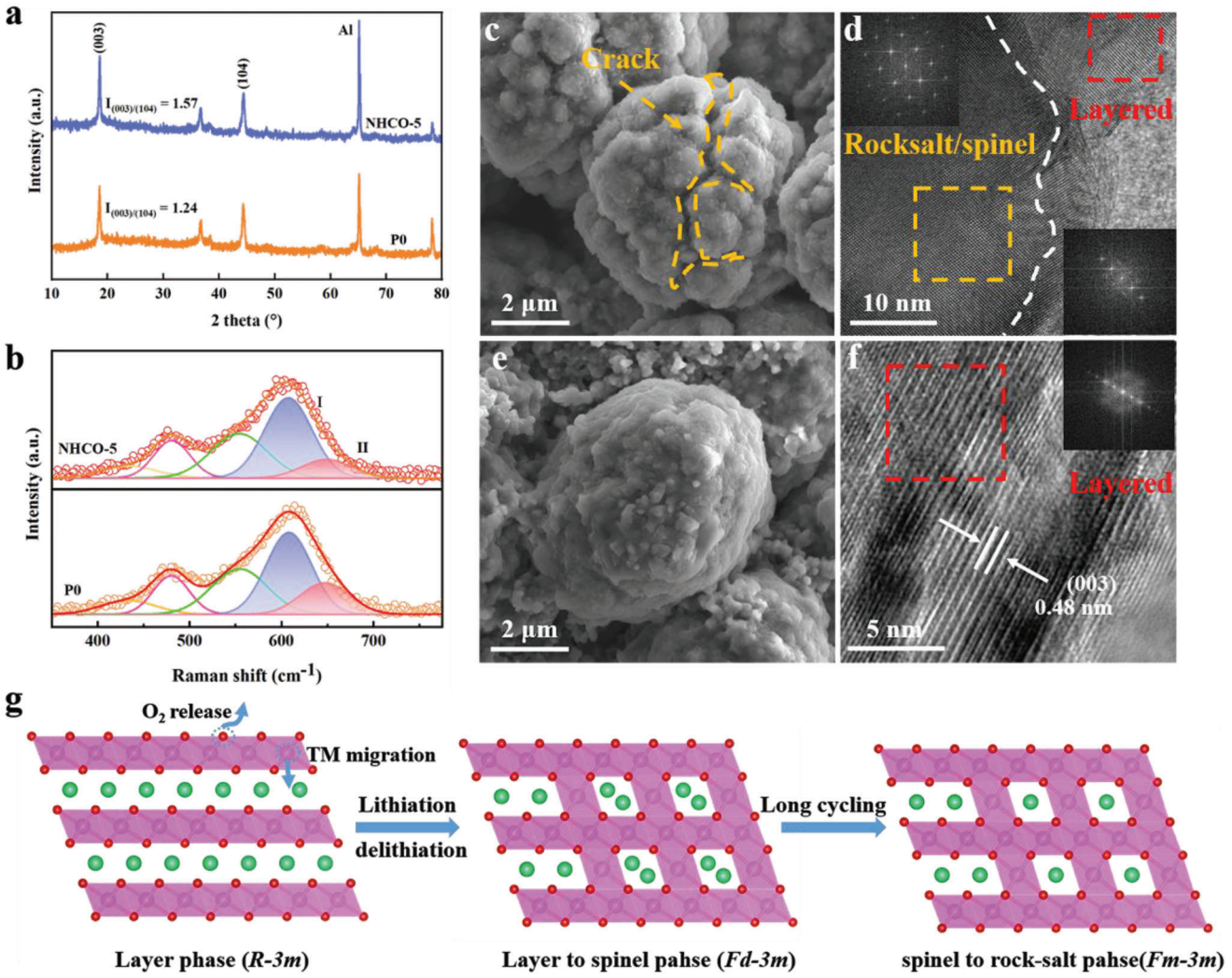

Figure 6. The analysis of P0 and NHCO-5 electrodes after 200 cycles: a) The comparison of XRD pattern. b) Raman spectra. The SEM images of c) P0 and e) NHCO-5. HRTEM images of d) P0 and f) NHCO-5. g) The schematic of the crystal structure deterioration for P0 electrode.

increasing electrical conductivity, facilitating lithium ion diffusion and fast charge transfer, but also suppressing oxygen release and promoting the charge compensation of both cationic and anionic redox.

To explore the structural evolution of P0 and NHCO-5 electrodes after 200 cycles, relevant characterizations were employed to study the changes of crystal structure and morphology. **Figure 6**a shows the comparison of XRD results for P0 and NHCO-5 electrodes after cycling. The value of $I_{(003)}/I_{(104)}$ for P0 is smaller than NHCO-5, indicating the higher degree of cation mixing due to the irreversible migration of transition metal ions.[17a] In addition, Raman spectroscopy was also used to detect the surface structural evolution after cycling and the corresponding results are displayed in Figure 6b. Two obvious peaks located at around 480 and 605 cm^{-1} contribute to the vibrations of the layered structure with R-3m spacing group.[33] A weak peak at about 430 cm^{-1} is assigned to the Li_2MnO_3 phase. The peak II at around 650 cm^{-1} of both samples is the evidence of the spinel/rock-salt structure due to the shortening of M–O bonds.[5b] The smaller area ratio of spinel-like component for NHCO-5 suggests that minor structural transformation occurs from layer to spinel/rock-salt phase. It is mainly ascribed to be the fact that surface defect and spinel-like phase can stabilize the crystal structure via suppressing oxygen release. What is more, the impedance changes of P0 and NHCO-5 electrodes after cycling are also detected, as shown in Figure S8a, Supporting Information. Compared with the EIS spectra of P0 and NHCO-5 electrodes before cycling, additional semicircle belonging to the impedance R_f of cathode–electrolyte interphase (CEI) appears in the middle-high frequency after cycling. According to the equivalent circuit, the corresponding fitting parameters are listed in Table S2, Supporting Information. The impedance of CEI film and the charge transfer for NHCO-5 electrode are 8.81 and 36.28 Ω after cycling, respectively, lower than P0 electrode (10.01 and 40.09 Ω), demonstrating better CEI film with low impedance and fast charge transfer for NHCO-5. The contents of Mn and Co elements deposited on the anode after cycling are quantitated by the ICP-MS. The corresponding results are shown in Figure

S8b, Supporting Information. Both P0 and NHCO-5 show the high content of Mn in comparison with Co, which demonstrates that Mn dissolves in the electrolyte more easily. In addition, the dissolution content of Mn and Co for the NHCO-5 electrode shows to be less than P0 electrode, indicating oxygen vacancies and integrated spinel-like phase can reduce the side reaction and dissolution of transition metals. SEM images of the cycled P0 and NHCO-5 electrodes are shown in Figures 6c,e, respectively. An obvious crack can be observed on the surface of P0 electrode, which is the result of continuing oxygen release, the formation of microscopic defects, and electrolyte corrosion.[34] In contrast, the NCHO-5 electrode still shows intact morphology. Enlarged TEM images of the P0 and NHCO-5 electrodes are shown in Figures 6d,f, respectively. The surface of P0 shows a mixed phase of layered phase (red box) and disorder rock-salt phase (Yellow box), which can be proved by the FFT images. The appearance of disordered rock-salt structure demonstrates the irreversible structural deterioration: first, the layered structure (*R–3m*) transforms to spinel-like phase (*Fd-3m*) and last, to inactive rock-salt phase (*Fm-3m*). This structural transformation occurs from the surface to bulk as shown in Figure 6g. Previous studies have proved that the irreversible lattice oxygen release and migration of transition metal ions mainly cause the structure deterioration and degradation of electrochemical performance.[35] In contrast, the clear lattice fringe of NHCO-5 electrode, corresponding to the (003) facet of *R3m* space structure, directly demonstrates the relatively intact layered structure after cycling. These results indicate the surface defect can suppress irreversible oxygen release, migration, and dissolution of transition metals and alleviate the side reaction for stabilizing the structure of LRMO.

3. Conclusion

In summary, a facile surface defect construction strategy is proved to address the issues of irreversible oxygen release and sluggish kinetic for Li-rich Mn-based oxides cathodes, resulting in the excellent rate performance and fast-charging capability with enhanced reversible anionic redox. The modified material NHCO-5 with appropriate oxygen vacancies and integrated spinel-like phase significantly exhibits outstanding electrochemical performance, including a high reversible specific capacity of 297.0 $mAh{\cdot}g^{-1}$ with 86.98% capacity retention after 100 cycles, high capacity of 180.7 $mAh{\cdot}g^{-1}$ at 5 C, and excellent fast-charging capability. Systematical characterization and theoretical calculation confirm that the surface defect can modulate the local electronic structure around Mn and O for suppressing oxygen release, irreversible migration of transition metals, and phase transformation. Moreover, the electrochemical activity of Li_2MnO_3 phase is largely stimulated with the synergistic function of reduced Mn and oxygen vacancies, resulting in both reversible anionic and cationic redox during cycling. The improved electrical conductivity, fast charge transfer, and existence of spinel-like phase with 3D Li^+ diffusion channels accelerates the kinetics of LRMO, contributing to the enhanced fast-charging capability. Therefore, we believe this work can provide new insight into enhancing fast-charging capability with reversible anionic redox for LRMO via the strategy of modulating local electronic structure.

Supporting Information

Supporting Information is available from the Wiley Online Library or from the author.

Acknowledgements

The authors acknowledge the financial support of the National Natural Science Foundation of China (52274309). This work also was supported by the Beamlines MCD–A and MCD–B (Soochow Beamline for Energy Materials) at NSRL.

Conflict of Interest

The authors declare no conflict of interest.

Data Availability Statement

The data that support the findings of this study are available from the corresponding author upon reasonable request.

Keywords

anionic redox, electronic structure modulation, fast-charging, Li-rich Mn-based oxides cathodes, oxygen vacancy

Received: April 12, 2023
Revised: May 22, 2023
Published online: June 21, 2023

[1] a) S. Li, H. Zhang, H. Li, S. Zhang, B. Zhu, S. Wang, J. Zheng, F. Liu, Z. Zhang, Y. Lai, *ACS Appl. Mater. Interfaces* **2021**, *13*, 39480; b) H. Zheng, Z. Hu, P. Liu, W. Xu, Q. Xie, W. He, Q. Luo, L. Wang, D. Gu, B. Qu, Z.-Z. Zhu, D.-L. Peng, *Energy Storage Mater.* **2020**, *25*, 76.

[2] Y. Li, L. Xie, Z. Zheng, Z.-W. Yin, J. Li, M. Weng, J. Liu, J. Hu, K. Yang, G. Qian, B. Cao, Z. Li, S. Xu, W. Zhao, S. Li, J. Sun, M. Zhang, F. Pan, *Nano Energy* **2020**, *77*, 105157.

[3] a) Y. Yang, G. Sun, Q. Zhu, Y. Jiang, W. Ke, P. Wang, Y. Zhao, W. Zhang, Z. Wang, *J. Mater. Chem. A* **2022**, *10*, 24018; b) J. Xu, J. Wan, W. Zhang, Y. Li, F. Cheng, Z. Cheng, Y. Xu, S. Sun, Q. Li, C. Fang, J. Han, *Adv. Funct. Mater.* **2023**, *33*, 2214613.

[4] a) J. Zhao, Y. Liang, X. Zhang, Z. Zhang, E. Wang, S. He, B. Wang, Z. Han, J. Lu, K. Amine, H. Yu, *Adv. Funct. Mater.* **2020**, *31*, 2009192; b) Y. Liu, H. Zhu, H. Zhu, Y. Ren, Y. Zhu, Y. Huang, L. Dai, S. Dou, J. Xu, C. J. Sun, X. L. Wang, Y. Deng, Q. Yuan, X. Liu, J. Wu, Y. Chen, Q. Liu, *Adv. Energy Mater.* **2021**, *11*, 2003479; c) M. Merz, B. Ying, P. Nagel, S. Schuppler, K. Kleiner, *Chem. Mater.* **2021**, *33*, 9534.

[5] a) C. Yan, Q. Shao, Z. Yao, M. Gao, C. Zhang, G. Chen, Q. Sun, W. Sun, Y. Liu, M. Gao, H. Pan, *Small* **2022**, *18*, 2107910; b) Z. Feng, H. Song, W. Su, M. Liu, Y. Li, R. Chen, S. Xu, Y. Lyu, D. Xiao, B. Guo, *Chem. Eng. J.* **2022**, *450*, 138114; c) G. Assat, D. Foix, C. Delacourt, A. Iadecola, R. Dedryvere, J. M. Tarascon, *Nat. Commun.* **2017**, *8*, 2219.

[6] a) J. Chen, H. Chen, Y. Mei, J. Gao, A. Dai, Y. Tian, W. Deng, G. Zou, H. Hou, C. E. Banks, T. Liu, K. Amine, X. Ji, *Energy Storage Mater.* **2022**, *52*, 736; b) Y. Fan, E. Olsson, G. Liang, Z. Wang, A. M. D'Angelo, B. Johannessen, L. Thomsen, B. Cowie, J. Li, F. Zhang, Y. Zhao, W. K. Pang, Q. Cai, Z. Guo, *Angew. Chem., Int. Ed.* **2022**, *62*, 202213806; c) Z. Li, S. Cao, C. Wu, H. Li, J. Chen, W. Guo, B. Chang, Y. Shen, Y. Bai, X. Wang, *J. Power Sources* **2022**, *536*, 231456.

[7] a) P. Liu, H. Zhang, W. He, T. Xiong, Y. Cheng, Q. Xie, Y. Ma, H. Zheng, L. Wang, Z. Z. Zhu, Y. Peng, L. Mai, D. L. Peng, *J. Am. Chem. Soc.* **2019**, *141*, 10876; b) Y. Bao, J. Wang, Y. Qian, Y. Deng, X. Yang, G. Chen, *Electrochim. Acta* **2020**, *330*, 135240.
[8] Y. Zhang, Z. Chen, X. Shi, C. Meng, P. Das, S. Zheng, F. Pan, Z. S. Wu, *Adv. Energy Mater.* **2022**, *13*, 2203045.
[9] a) Y. Pei, Q. Chen, M. Wang, B. Li, P. Wang, G. Henkelman, L. Zhen, G. Cao, C.-Y. Xu, *Nano Energy* **2020**, *71*, 104644; b) Z. Huang, T. Xiong, X. Lin, M. Tian, W. Zeng, J. He, M. Shi, J. Li, G. Zhang, L. Mai, S. Mu, *J. Power Sources* **2019**, *432*, 8; c) D. Luo, X. Ding, J. Fan, Z. Zhang, P. Liu, X. Yang, J. Guo, S. Sun, Z. Lin, *Angew. Chem., Int. Ed.* **2020**, *59*, 23061.
[10] G. Zhang, M. Chen, C. Li, B. Wu, J. Chen, W. Xiang, X. Wen, D. Zhang, G. Cao, W. Li, *Chem. Eng. J.* **2022**, *443*, 136434.
[11] S. L. Xianggang Gao, H. Zhang, S. Zhang, S. Chang, H. Li, S. Li, Y. Lai, Zhian Zhang, *Mater. Today Energy* **2022**, *30*, 101152.
[12] L. Bao, L. Wei, N. Fu, J. Dong, L. Chen, Y. Su, N. Li, Y. Lu, Y. Li, S. Chen, F. Wu, *J. Energy Chem.* **2022**, *66*, 123.
[13] Z. Ye, B. Zhang, T. Chen, Z. Wu, D. Wang, W. Xiang, Y. Sun, Y. Liu, Y. Liu, J. Zhang, Y. Song, X. Guo, *Angew. Chem., Int. Ed.* **2021**, *60*, 23248.
[14] Z. Lin, L. Dong, H. Xie, F. Tan, X. Ding, J. Cui, X. Xie, C. Liu, *Angew. Chem., Int. Ed.* **2022**, *61*, 202203698.
[15] a) P. Zhang, Y. He, H. Huang, B. Chen, X. Zhai, J. Zhou, J. Dong, Z. Guo, *Appl. Surf. Sci.* **2021**, *554*, 149626; b) Z. Chen, J. Meng, Y. Wang, Q. Ma, F. Lai, Z. Li, Q. Zhang, D. Li, S. Zhong, *Electrochim. Acta* **2021**, *378*, 138138.
[16] a) W. He, F. Ye, J. Lin, Q. Wang, Q. Xie, F. Pei, C. Zhang, P. Liu, X. Li, L. Wang, B. Qu, D. L. Peng, *Nano-Micro Lett.* **2021**, *13*, 205; b) W. Wang, W. Cheng, Y. Huang, Y. Wang, Y. Wei, Q. Liu, *Appl. Surf. Sci.* **2022**, *605*, 154819.
[17] a) C. Zheng, Z. Yang, J. Feng, J. Zhong, Z. Wei, J. Li, *J. Mater. Chem. A* **2022**, *10*, 16046; b) X. Ding, D. Luo, J. Cui, H. Xie, Q. Ren, Z. Lin, *Angew. Chem.* **2020**, *132*, 7852; c) Z. Li, H. Li, S. Cao, W. Guo, J. Liu, J. Chen, C. Guo, G. Chen, B. Chang, Y. Bai, X. Wang, *Chem. Eng. J.* **2022**, *452*, 139041.
[18] W. Guo, C. Zhang, Y. Zhang, L. Lin, W. He, Q. Xie, B. Sa, L. Wang, D. L. Peng, *Adv. Mater.* **2021**, *33*, 2103173.
[19] Q. X. Ma, Z. J. Chen, S. W. Zhong, J. X. Meng, F. L. Lai, Z. F. Li, C. Cheng, L. Zhang, T. F. Liu, *Nano Energy* **2021**, *81*, 105622.
[20] B. Qiu, M. Zhang, L. Wu, J. Wang, Y. Xia, D. Qian, H. Liu, S. Hy, Y. Chen, K. An, Y. Zhu, Z. Liu, Y. S. Meng, *Nat. Commun.* **2016**, *7*, 12108.
[21] a) Q. Li, Ning, D. W., K. An, Y. Tang, D. Zhou, G. Schuck, Z. Chen, N. Zhang, X. Liu, *Nat. Commun.* **2022**, *13*, 1123; b) T. Lin, T. U. Schulli, Y. Hu, X. Zhu, Q. Gu, B. Luo, B. Cowie, L. Wang, *Adv. Funct. Mater.* **2020**, *30*, 1909192.
[22] W. He, C. Zhang, M. Wang, B. Wei, Y. Zhu, J. Wu, C. Liang, L. Chen, P. Wang, W. Wei, *Adv. Funct. Mater.* **2022**, *32*, 2200322.
[23] Y. Kang, X. Guo, Z. Guo, J. Li, Y. Zhou, Z. Liang, C. Han, X. He, Y. Zhao, N. Tavajohi, B. Li, *J. Energy Chem.* **2021**, *62*, 538.
[24] X. Wu, Y. Bai, Z. Li, J. Liu, K. Zhao, Z. Du, *J. Energy Chem.* **2021**, *56*, 121.
[25] J. Hwang, S. Myeong, W. Jin, H. Jang, G. Nam, M. Yoon, S. H. Kim, S. H. Joo, S. K. Kwak, M. G. Kim, J. Cho, *Adv. Mater.* **2020**, *32*, 2001944.
[26] C. Huang, Z. Wang, H. Wang, D. Huang, Y.-b. He, S.-X. Zhao, *Mater. Today Energy* **2022**, *29*, 101116.
[27] B. Xu, C. R. Fell, M. Chi, Y. S. Meng, *Energy Environ. Sci.* **2011**, *4*, 2223.
[28] X.-Y. Li, F. Yu, W. Ke, Y.-S. Jiang, l. Que, L. Zhao, S.-E. Hao, Z.-B. Wang, *J. Mater. Chem. A* **2023**, *11*, 2252.
[29] a) K. Chai, J. Zhang, Q. Li, D. Wong, L. Zheng, C. Schulz, M. Bartkowiak, D. Smirnov, X. Liu, *Small* **2022**, *18*, 2201014; b) D. Dixon, S. Mangold, M. Knapp, H. Ehrenberg, A. Bhaskar, *Adv. Energy Mater.* **2021**, *11*, 2100479.
[30] G.-J. Xu, W. Ke, F.-D. Yu, J. Feng, Y.-S. Jiang, L.-F. Que, L. Zhao, Z.-B. Wang, *J. Energy Chem.* **2022**, *75*, 117.
[31] Q. Li, D. Ning, D. Zhou, K. An, D. Wong, L. Zhang, Z. Chen, G. Schuck, C. Schulz, Z. Xu, G. Schumacher, X. Liu, *J. Mater. Chem. A* **2020**, *8*, 7733.
[32] Z. Lun, B. Ouyang, D. A. Kitchaev, R. J. Clément, J. K. Papp, M. Balasubramanian, Y. Tian, T. Lei, T. Shi, B. D. McCloskey, J. Lee, G. Ceder, *Adv. Energy Mater.* **2018**, *9*, 1802959.
[33] Y. C. Zhuo Yao, C. Liu, H. Chen, S. Wu, D. Luo, Z. Lin, S. Zhang, *J. Energy Chem.* **2023**, *82*, 513.
[34] L. Zeng, H. Liang, B. Qiu, Z. Shi, S. Cheng, K. Shi, Q. Liu, Z. Liu, *Adv. Funct. Mater.* **2023**, 2213260.
[35] a) Z. Feng, H. Song, Y. Li, Y. Lyu, D. Xiao, B. Guo, *ACS Appl. Mater. Interfaces* **2022**, *14*, 5308; b) J. Yang, P. Li, F. Zhong, X. Feng, W. Chen, X. Ai, H. Yang, D. Xia, Y. Cao, *Adv. Energy Mater.* **2020**, *10*, 1904264.